

Electrochemical CO₂ reduction to ethylene by ultrathin CuO nanoplate arrays

Wei Liu¹, Pengbo Zhai², Aowen Li^{3,4}, Bo Wei¹, Kunpeng Si¹, Yi Wei^{5,6}, Xingguo Wang¹, Guangda Zhu⁷, Qian Chen¹, Xiaokang Gu¹, Ruifeng Zhang¹, Wu Zhou^{id}^{3,4,8} & Yongji Gong^{id}^{1,9}✉

Electrochemical reduction of CO₂ to multi-carbon fuels and chemical feedstocks is an appealing approach to mitigate excessive CO₂ emissions. However, the reported catalysts always show either a low Faradaic efficiency of the C₂₊ product or poor long-term stability. Herein, we report a facile and scalable anodic corrosion method to synthesize oxygen-rich ultrathin CuO nanoplate arrays, which form Cu/Cu₂O heterogeneous interfaces through self-evolution during electrocatalysis. The catalyst exhibits a high C₂H₄ Faradaic efficiency of 84.5%, stable electrolysis for ~55 h in a flow cell using a neutral KCl electrolyte, and a full-cell ethylene energy efficiency of 27.6% at 200 mA cm⁻² in a membrane electrode assembly electrolyzer. Mechanism analyses reveal that the stable nanostructures, stable Cu/Cu₂O interfaces, and enhanced adsorption of the *OCCOH intermediate preserve selective and prolonged C₂H₄ production. The robust and scalable produced catalyst coupled with mild electrolytic conditions facilitates the practical application of electrochemical CO₂ reduction.

¹School of Materials Science and Engineering, Beihang University, Beijing 100191, China. ²College of Physics, Qingdao University, Qingdao 266071, China. ³School of Physical Sciences, University of Chinese Academy of Sciences, Beijing 100049, China. ⁴CAS Key Laboratory of Vacuum Physics, University of Chinese Academy of Sciences, Beijing 100049, China. ⁵State Key Laboratory of Organic-Inorganic Composites, Beijing University of Chemical Technology, Beijing 100029, China. ⁶Beijing Key Laboratory of Electrochemical Process and Technology for Materials, Beijing University of Chemical Technology, Beijing 100029, China. ⁷Beijing National Laboratory for Molecular Sciences, Laboratory of Polymer Physics and Chemistry, Institute of Chemistry, Chinese Academy of Sciences, Beijing 100190, China. ⁸CAS Center for Excellence in Topological Quantum Computation, University of Chinese Academy of Sciences, Beijing 100049, China. ⁹Center for Micro-Nano Innovation of Beihang University, Beijing 100191, China. ✉email: yongjigong@buaa.edu.cn

The depletion of fossil fuels and their non-renewability continue to emphasize the importance of utilizing renewable energy to convert carbon dioxide (CO₂) into fuels and chemical feedstocks^{1–3}. Artificial conversion of CO₂ is essential to reduce its emissions and realize the sustainable development of humanity^{3,4}. The electrochemical CO₂ reduction reaction (CO₂RR) is the most attractive method due to its mild reaction conditions and capacity for renewable electricity storage⁵. Among the products of the CO₂RR, low-value C₁ species such as carbon monoxide (CO) and formate (HCOO[−]) are the most common products due to the sluggish kinetics of the C–C coupling reaction^{6,7}. As shown by previous studies, the C–C coupling reaction is the vital step for C₂₊ species formation^{8–11}. Theoretical calculations reveal that excessively strong or weak binding of *CO intermediates is unfavorable for the generation of C₂₊ species^{9,12–14}. Copper-based (Cu-based) materials possessing a moderate adsorption energy of the *CO intermediate have been the most efficient catalysts in converting CO₂ to C₂₊ hydrocarbons and oxygenates with considerable activity^{2,15–18}. The CO₂RR to ethylene (C₂H₄) with high current density and Faradic efficiency (FE) is intensively studied because of the extremely high industrial value and limited sources of C₂H₄^{18–21}. However, as multi-step electron and proton transfer processes are involved in C₂H₄ formation, hydrogen (H₂) and other by-products such as methane (CH₄) will inevitably be produced during electrolysis^{16,20,22–24}. Therefore, the activity and selectivity of C₂H₄ formation are still limited for Cu-based catalysts.

Various procedures such as facet and grain boundary regulation^{25–27}, morphology engineering^{18,28–32}, electrode surface additive modification^{14,33–36}, electrolyte design^{37,38} and oxide-derived catalysis^{16,20,39–42} have been proposed to improve the current density and FE of C₂H₄ production. Among these catalysts, oxide-derived Cu (OD-Cu) has the highest product ratio of C₂H₄ to CH₄^{21,26,40}. These catalysts have generally been synthesized by thermal oxidation and subsequently reduced through H₂ annealing or in situ electrolysis. Hemma et al. revealed that the increased local pH caused by the rough morphology of OD-Cu suppressed CH₄ formation²¹. The existence of Cu⁺ species may promote the adsorption of CO₂RR intermediates, which is crucial to improve the C₂H₄ selectivity²¹. Although the existence and important role of Cu⁺ species in the CO₂RR have been proven by many in situ and *operando* tests (Raman spectroscopy, X-ray absorption spectroscopy, etc.)^{20,26,43,44}, thermal oxidation treatments usually result in a disordered morphology and an inadequate amount of oxidation species⁴⁰. These issues lead to the disappearance of Cu/Cu^{δ+} heterointerfaces during long-term electrocatalysis tests due to the self-evolution of surface species and morphologies. Therefore, constructing stable Cu/Cu^{δ+} heterointerfaces with exquisite nanostructures is highly desirable to improve the stability of C₂H₄ production.

Here, we report the preparation of an OD-Cu catalyst with a dense vertical lamellate Cu nanostructure (denoted as DVL-Cu). The DVL-Cu catalyst was obtained via in situ electrochemical reduction of CuO ultrathin nanoplate arrays (denoted as CuO-NPs) synthesized by galvanostatic anodic oxidation in an alkaline solution. The electrochemical CO₂RR test of DVL-Cu delivered an C₂H₄ FE of 73.6% and a total C₂₊ (mainly ethylene and ethanol) FE of >80% at −0.8 V vs. the reversible hydrogen electrode (RHE), all potentials are with respect to this reference in this article) in an H-cell and an even higher C₂H₄ FE of 84.5% in a flow cell, with neutral potassium chloride (KCl) as the catholyte. Moreover, the catalyst achieved an ethylene energy efficiency (EE_{C₂H₄}) of 28.9% and ~55 h stable long-term electrolysis in a flow cell. The experimental and simulation results reveal that the nanostructured DVL-Cu generated Cu/Cu₂O heterogeneous interfaces and dispersed the electrode current density effectively to avoid

agglomeration during the CO₂RR. Meanwhile, the KCl electrolyte impedes the dissolution/redeposition of Cu⁺ species due to its high local pH microenvironment and suppresses hydrogen evolution at higher overpotentials, which favors the high selectivity and stability of the DVL-Cu catalyst. Density functional theory (DFT) calculations suggest that the Cu/Cu₂O interfaces in DVL-Cu facilitate C₂H₄ formation due to their reduced C–C dimerization energy in the C₂H₄ formation pathway. The facile synthetic method, mild electrolysis conditions (neutral electrolyte), and prolonged electrolysis stability make this material a promising candidate for commercial CO₂RR catalysts in the future.

Results

Preparation and characterization of the DVL-Cu catalyst. First, CuO-NPs were synthesized by galvanostatic anodic oxidation of Cu foil in a 1 M sodium hydroxide (NaOH) electrolyte. Copper hydroxide (Cu(OH)₂) was primarily generated on the Cu surface during anodic oxidation⁴⁵, while Cu(OH)₂ spontaneously converted to CuO at a proper current density. We found that 0.26 mA cm^{−2} (calculated based on the geometric area) was the most suitable current density for CuO-NPs synthesis, resulting in the best catalyst performance. Excessive current with rapid Cu(OH)₂ production led to the complete coverage of blue Cu(OH)₂ on the surface, and an insufficient current generated only a thin oxide layer rather than nanoplate arrays.

A schematic illustration of the CuO-NPs formation process is displayed in Fig. 1a. This process can be divided into three stages: the Cu etching stage, CuO nucleation stage and CuO growth stage. The Cu surface was first corroded by a positive bias at the etching stage (Fig. 1b). Once Cu²⁺ was saturated in the solution, CuO nucleated and grew on the surface as Cu(OH)₂ was generated and dehydrated (Supplementary Fig. 1). The surface oxygen content no longer increased after the nucleation stage, indicating that the surface had been completely covered by the oxide layer (Fig. 1c). Eventually, vertically arranged and densely stacked CuO-NPs were synthesized. The successful synthesis of CuO-NPs on a large piece of Cu foil (25 × 25 cm²) by this method proves the scalability to prepare catalysts for industrial applications (Supplementary Figs. 2–4, the samples used for characterization were obtained from Cu foils with a size of 1.5 × 3 cm² unless otherwise specified). The morphology and atomic structure of an individual CuO nanoplate before and after the CO₂RR can be characterized in detail after sonication. As shown by transmission electron microscopy (TEM) images, the CuO nanoplates are composed of polygonal ultrathin CuO nanosheets (Fig. 1d and Supplementary Fig. 5). The nm-scale thickness of the CuO nanosheets was confirmed by atomic force microscopy (AFM), showing that the thicknesses of the corresponding layers are 3.136 and 0.782 nm, respectively (Fig. 1e). The ultrathin thickness of CuO nanosheets leads to ultrafine Cu nanostructures with numerous exposed catalytically active sites during electrocatalysis. Specifically, the thickness of the whole CuO-NPs layer on Cu foil is 2.25 μm, as measured by the scanning electron microscopy (SEM) cross-sectional image (Supplementary Fig. 6), which also exhibits a uniform and compact stacking pattern. Furthermore, this three-dimensional self-supporting structure is beneficial to mass transfer and the exposure of catalytically active sites. In addition, the CuO-NPs were thermally reduced under Ar/H₂ to obtain reduced-CuO-NPs (denoted as R-CuO-NPs, Supplementary Fig. 7) as a control group to test the CO₂RR performance.

The DVL-Cu catalyst was produced during the in situ electrochemical CO₂RR by self-evolution in a gas-tight H-cell (Fig. 2a). CuO-NPs were used as the working electrode, a

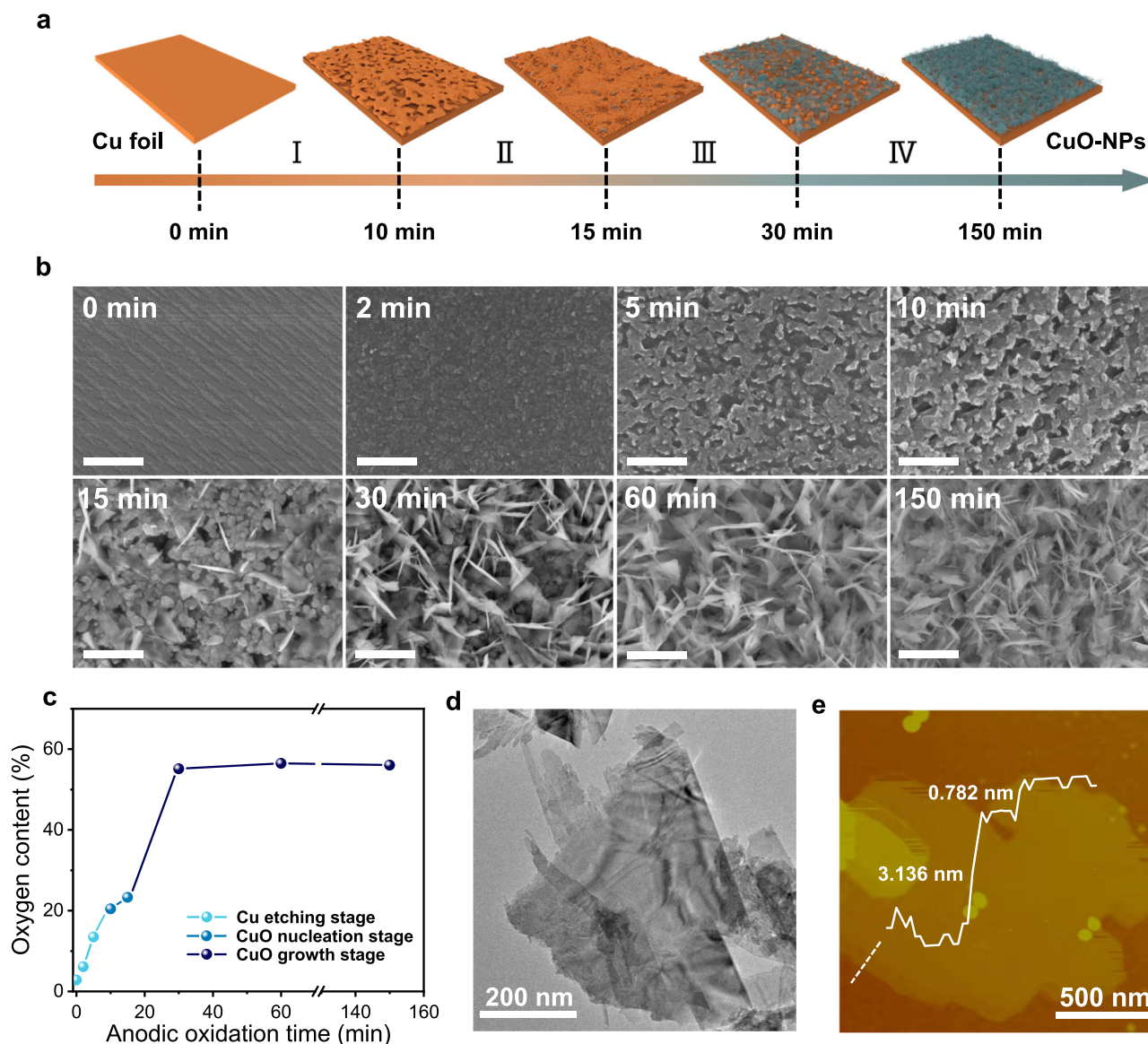


Fig. 1 Preparation and characterization of CuO-NPs. **a** Schematic illustration of the preparation of CuO-NPs. **b** SEM images of Cu foils at different anodic oxidation times. The scale bars are 500 nm. **c** Oxygen content of the Cu surface at different anodic oxidation times. **d** TEM image of the CuO-NPs. **e** AFM image of the CuO-NPs and the corresponding height profile from the dashed line.

Ag/AgCl electrode was used as the reference electrode (RE), and platinum foil was employed as the counter electrode. In situ galvanostatic reduction was performed at -0.8 V under a CO_2 atmosphere. The black foil quickly turned rufous after 20 s of electrolysis (Supplementary Fig. 8), suggesting that the CuO-NPs were reduced to a lower valence. After 20 min of electrolysis, the vertically arranged and densely stacked laminated nanostructure was retained (Fig. 2b, c, and Supplementary Figs. 9, 10). However, every single piece of ultrathin CuO nanoplate was converted to a thicker nanoplate composed of small nanoparticles. These nanoparticles were considered active catalytic sites for C_2H_4 formation, as suggested by a previous study⁴⁶. This nanoplate-like morphology suppresses the agglomeration of Cu nanoparticles, which benefits the long-term catalytic stability. The curves depicted in Fig. 2d present the grazing incident X-ray diffraction (GI-XRD) results of the original CuO-NPs and DVL-Cu after different reduction times. The GI-XRD result of CuO-NPs shows the successful synthesis of CuO without any other impurities (such as $\text{Cu}(\text{OH})_2$ and Cu_2O). The peaks ascribed to cuprite-type

Cu_2O begin to appear after 20 s of electrochemical reduction. The CuO peaks completely disappear after 1 min of electrochemical reduction, while the peak of Cu_2O still remains even when the reduction time is extended to 2 h, which is consistent with previous studies on OD-Cu catalysts^{20,26,45,46}. Comparing the line for the 2 h reduction time and that for the 5 min reduction time, the peak intensity of the Cu(110) facet increases with the duration of electrolysis. As Cu(111) is the most thermodynamically stable facet in polycrystalline Cu²⁶, the increased ratio of Cu(110) might result from the stabilizing effect of CO_2RR intermediates²⁶.

Supplementary Figs. 11, 12 and Fig. 2e show X-ray photoelectron spectroscopy (XPS) and Auger electron spectroscopy (AES) results of CuO-NPs and DVL-Cu (taken after 1 h of electrolysis) for different Ar^+ beam etching times, noting that the Ar^+ beam could etch the surface of the sample to reveal subsurface information. The typical satellite peak and Cu LMM Auger peak location (971.3 eV) of the CuO-NPs indicate the characteristics of Cu^{2+} species²⁰. No satellite peak was found in the DVL-Cu XPS

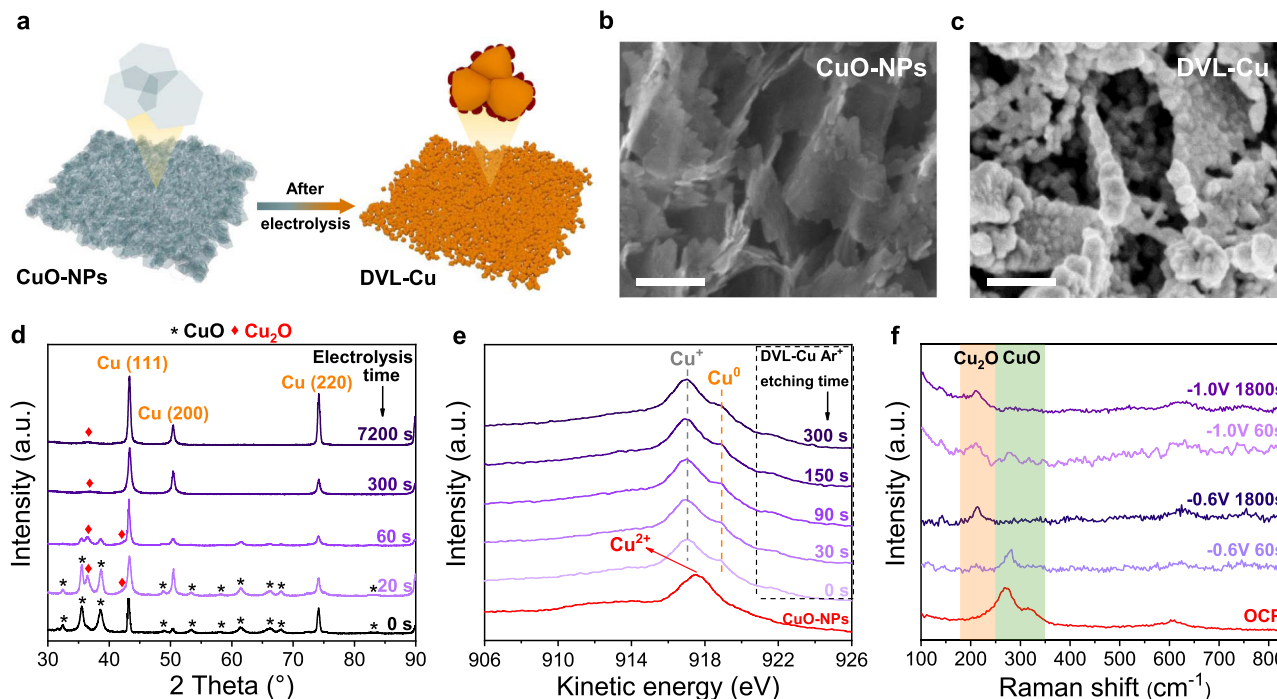


Fig. 2 Preparation and characterization of DVL-Cu. **a** Schematic illustration of morphology changes during the electrochemical reduction of DVL-Cu and CuO-NPs. **b, c** High-magnification SEM images of CuO-NPs (**b**) and DVL-Cu (**c**). The scale bars are 200 nm. **d** GI-XRD patterns of CuO-NPs and DVL-Cu for different reduction times. **e** Cu LMM Auger spectra of CuO-NPs and DVL-Cu (after 1 h reduction) with respect to different Ar⁺ etching times. **f** In situ Raman spectra of DVL-Cu during electrolysis.

results for different etching times, suggesting that the original Cu²⁺ species in the CuO-NPs are completely reduced after electrolysis. Cu Auger LMM spectra demonstrate that Cu⁰ and Cu⁺ species co-exist in DVL-Cu even after 300 s of Ar⁺ beam etching (the etching depth was estimated to be 50 nm), which could entirely remove the surface oxide layer formed by air oxidation (usually < 5 nm). In situ Raman spectroscopy was further performed to identify the valence of Cu during electrolysis (Fig. 2f and Supplementary Fig. 13). At the open-circuit potential (OCP), peaks located at 286, 327 and 618 cm⁻¹ were ascribed to CuO. CuO characteristic peaks weakened, and peaks associated with Cu₂O began to appear when DVL-Cu was electrolyzed at -0.6 V for 60 s. When the electrolysis was carried out at -0.6 V for 1800 s, the peaks of Cu₂O still existed, but those of CuO completely disappeared. These results were similar for electrolysis at a higher overpotential of -1.0 V, except that the peak intensity of Cu₂O was lower than that at -0.6 V. Thus, it was concluded that Cu⁺ species were preserved during the electrochemical CO₂RR, which might be due to stabilization effects generated by the high local pH and Cl⁻^{16,21}.

Additionally, aberration-corrected scanning transmission electron microscopy (STEM) combined with electron energy-loss spectrometry (EELS) was performed to reveal the valence states and distribution of Cu species in DVL-Cu (Fig. 3 and Supplementary Fig. 14). The structure of a large particle decorated by several small particles is displayed in the bright-field (BF) image (Fig. 3a). The fast Fourier transform (FFT) patterns of the central large particle (#1) and a surrounding small particle (#2) are consistent with the Cu[110] and Cu₂O[110] zone axes, respectively. Cu(111) and (002) facets were delineated in the enlarged image of area #1 (Fig. 3b). Energy-loss near-edge fine structure (ELNES) analysis, which is a commonly applied method to determine the valence state of 3d metal elements, was also performed on the DVL-Cu sample to confirm its composition and distribution⁴⁷. The fine structures of the EELS spectrum

extracted from area #1 are consistent with Cu⁰, while the spectrum from area #2 is related to Cu⁺, matching well with the FFT analysis (Fig. 3c). Cu valence state mapping based on EELS spectrum imaging shows the distribution of Cu and Cu₂O in the whole area (Fig. 3d). The dashed lines highlighted in the overlay of the Cu and Cu₂O maps indicate the existence of Cu/Cu₂O interfaces on DVL-Cu, which might be beneficial for the CO₂RR.

Electrochemical CO₂RR performance in the H-cell. To measure the electrochemical CO₂RR performance of DVL-Cu, we performed electrolysis in CO₂-saturated 0.5 M KCl by using a gas-tight H-cell. For comparison, the electrochemical CO₂RR performance of the R-CuO-NPs was also evaluated under the same conditions. It is worth noting that KCl was chosen as the electrolyte because it benefits the preservation of Cu₂O during the CO₂RR through a high local pH, and the specific adsorption of Cl⁻ suppresses hydrogen evolution at higher overpotentials^{48,49}.

The geometric current density of DVL-Cu in the CO₂-saturated electrolyte is considerably higher than that of R-CuO-NPs over the whole test potential window (Supplementary Fig. 15), while the two catalysts deliver similar geometric current densities in the Ar-saturated electrolyte, indicating that DVL-Cu possesses higher intrinsic CO₂RR activity. To exclude the electrochemical surface area (ECSA) influence, we calculated the roughness factor (RF) of the two samples by the double-layer capacitance method (Supplementary Fig. 17). DVL-Cu has an RF of 201.7, while R-CuO-NPs have a comparable RF of 165.7. These measurements eliminate the influence of the ECSA and confirm the higher intrinsic CO₂RR activity of DVL-Cu than R-CuO-NPs. Moreover, DVL-Cu exhibits high C₂H₄ and FE_{C₂+} FE, which shows a higher FE_{C₂H₄} of 74.9 ± 2.6% and FE_{C₂+} of 80.5 ± 2.3% at -0.9 V (Fig. 4a and Supplementary Table 3) than that of R-CuO-NPs (FE_{C₂H₄} = 52.0 ± 3.7%, FE_{C₂+} = 61.9 ± 4.0%) (Fig. 4b). The liquid products of DVL-Cu and R-CuO-NPs are mainly composed

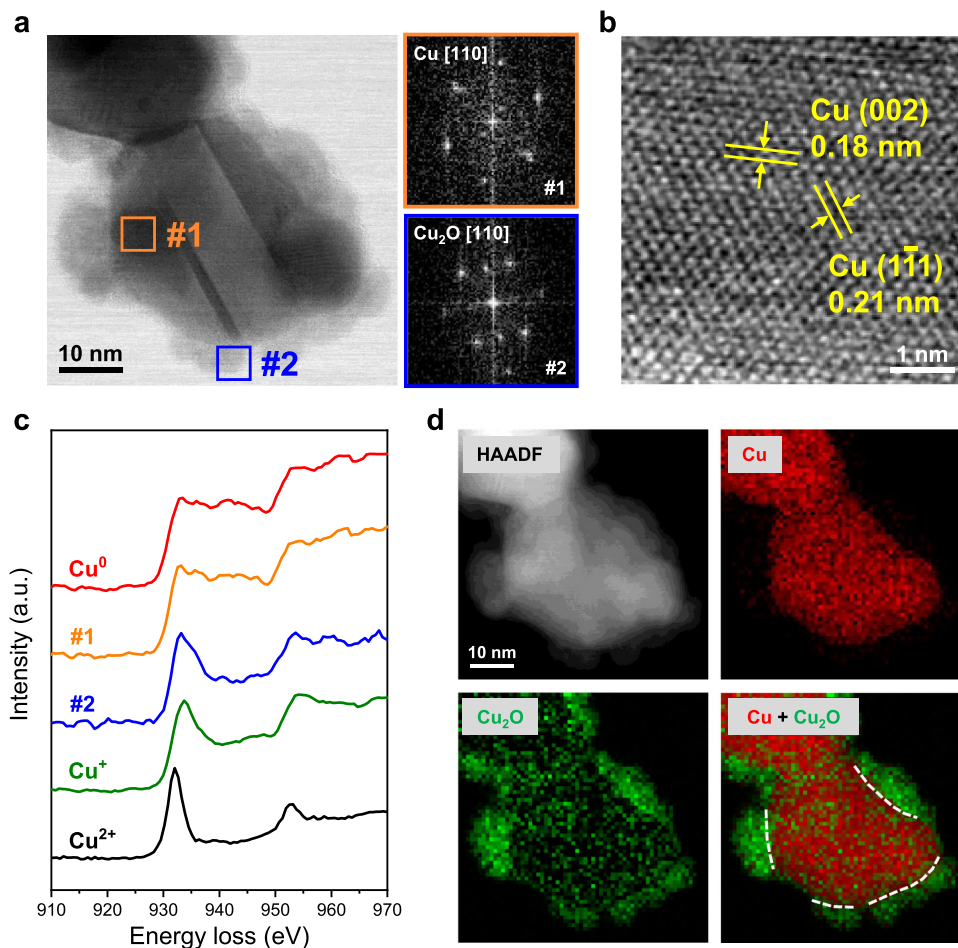


Fig. 3 STEM and EELS characterizations of the DVL-Cu catalyst. **a** STEM BF image (left) of DVL-Cu and FFT patterns (right) of the corresponding area in the BF image. **b** Enlarged image of area #1 in (a). **c** EELS spectra acquired from areas #1 and #2 in (a). Standard Cu, Cu⁺ and Cu²⁺ EELS results are plotted as references. **d** STEM high-angle annular dark-field (HAADF) image and EELS maps of Cu and Cu₂O and their overlay in DVL-Cu. The dashed lines highlighted in the overlay denote the Cu/Cu₂O interfaces.

of ethanol and formate, with a small percentage of acetate, propanol, etc. (Fig. 4e). Furthermore, the FE_{H₂} is only 13.6% at −0.9 V of DVL-Cu, which might be due to the massive consumption of H atoms in the proton-coupled electron transfer (PCET) step during the CO₂RR. Additionally, the partial current density curves and C₂H₄ Tafel curves were plotted to reveal the kinetic characteristics. The C₁ partial current densities of these two catalysts are comparable, but the C₂₊ partial current density of DVL-Cu is five times higher than that of R-CuO-NPs at −1.0 V (Fig. 4c). The C₂H₄ Tafel slopes of DVL-Cu and R-CuO-NPs are 179.3 mV decade^{−1} and 421.1 mV decade^{−1} (Fig. 4d), respectively, suggesting a much lower C₂H₄ formation kinetic barrier on DVL-Cu than on R-CuO-NPs. The sluggish kinetics of C₂H₄ and C₂₊ formation on R-CuO-NPs was further confirmed by the C₂₊/C₁ (CO, formate) and C₂H₄/CH₄ ratios in CO₂RR products (Fig. 4f). The C₂₊/C₁ and C₂H₄/CH₄ product ratios of DVL-Cu at −0.8 V are 19.4 and 208.6, respectively, indicating that most of the CO intermediates tend to dimerize, generating C₂₊ products rather than forming C₁ species. In comparison, the C₂₊/C₁ and C₂H₄/CH₄ product ratios (3.6 and 7.0 at −0.8 V) on R-CuO-NPs are much lower than that of DVL-Cu, which verifies the sluggish kinetics of the C–C coupling step on R-CuO-NPs.

The performance observed in stability tests with OD-Cu catalysts was always unsatisfactory according to previous studies. We performed long-term electrolysis under potentiostatic mode with the same conditions mentioned above (Supplementary

Figs. 16 and 18). DVL-Cu shows a steady *i*-*t* curve and high C₂H₄ selectivity (FE_{C₂H₄} = 62.2%) for 50 h at −0.8 V. In contrast, R-CuO-NPs only retains a stable FE_{C₂H₄} for less than 7 h at −0.8 V. Post-electrolysis SEM images of DVL-Cu show that nanoplates densely stack in order without any agglomeration after 50 h of electrolysis, and only a slight increase in plate thickness is observed (Supplementary Figs. 25a and b). The poor stability of R-CuO-NPs might be caused by the agglomeration of Cu nanoparticles during the CO₂RR (Supplementary Fig. 19).

Additionally, the high-resolution transmission electron microscopy (HRTEM) images confirm that there are no Cu₂O species in R-CuO-NPs after 2 h of the CO₂RR, either at the edge or the center (Supplementary Fig. 20), and the exposed plane is similar to that of DVL-Cu. Cu₂O characteristic peaks are also absent in the GI-XRD profiles of R-CuO-NPs after 1 h of the CO₂RR (Supplementary Fig. 21). However, the DVL-Cu sample preserves a similar Cu/Cu₂O composite structure and subsurface Cu⁺ content after a long-term test (Supplementary Figs. 27–29). The presence of Cu₂O in DVL-Cu may be the origin of the CO₂RR performance under the premise that the ECSA, exposed Cu facets, and hydrophilicity (Supplementary Fig. 30) of these two catalysts are comparable.

Electrochemical CO₂RR performance in the flow cell and MEA electrolyzer. To evaluate the application potential of CuO-NPs for the industrial CO₂RR, we further measured their catalytic performance in a flow cell. A Cu membrane (500 nm) was

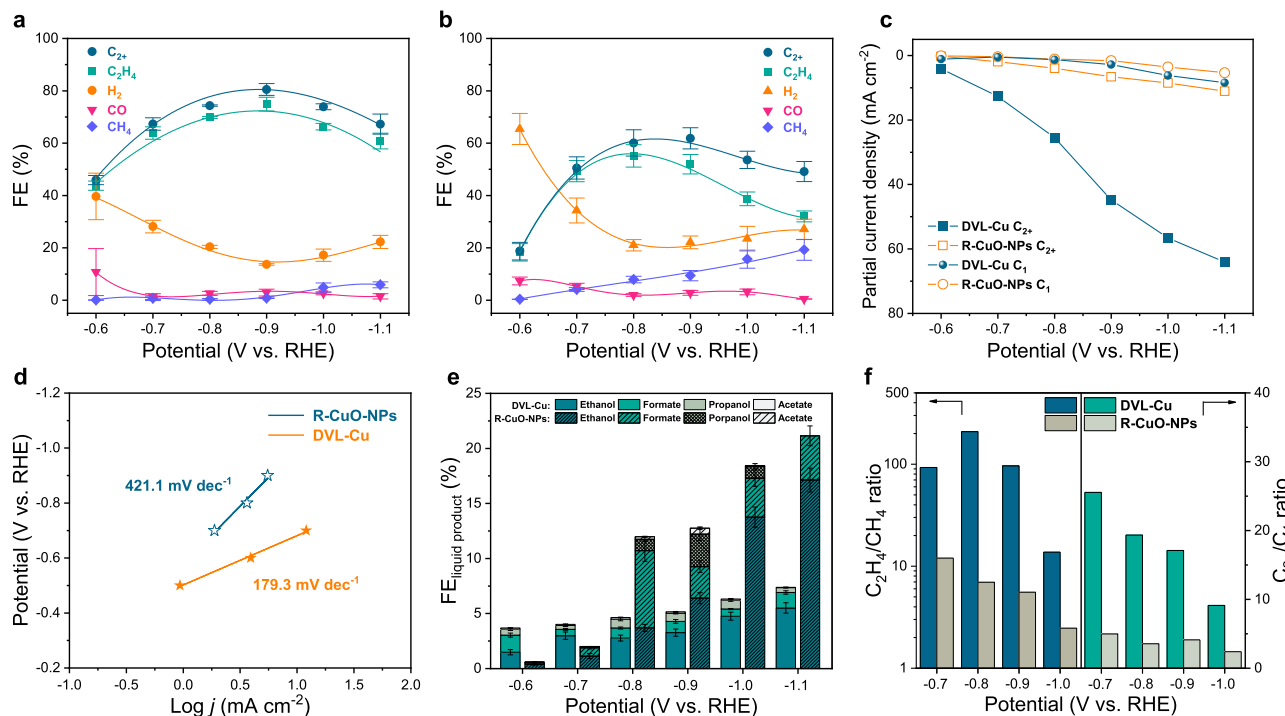


Fig. 4 Electrochemical CO₂RR performance of DVL-Cu and R-CuO-NPs. **a** FEs of DVL-Cu. **b** FEs of R-CuO-NPs. **c** C₂₊ and C₁ partial current densities of DVL-Cu and R-CuO-NPs. **d** C₂H₄ partial current density Tafel plots of DVL-Cu and R-CuO-NPs. **e** FEs of liquid products of DVL-Cu and R-CuO-NPs. **f** C₂H₄/CH₄ ratios and C₂₊/C₁ ratios for CO₂RR products of DVL-Cu and R-CuO-NPs. Error bars represent the standard deviation of three independent measurements.

deposited on carbon paper (Sigracet 28BC) with a gas diffusion layer (GDL) by electron beam evaporation (Fig. 5a). Then, galvanostatic anodic oxidation was performed to obtain CuO-NPs on the GDL (CuO-NPs@GDL), similar to those on copper foil. The synthesis and characterization details can be seen in the supplementary information (Methods and Supplementary Figs. 32 and 33). The as-fabricated electrode was utilized in a flow cell setup reported previously (Supplementary Figs. 34 and 35), where KCl and KOH served as the catholyte and anolyte, respectively. CuO nanoplates on the GDL were converted to DVL-Cu during the CO₂RR with a maintained plate-like nanostructure (DVL-Cu@GDL, Supplementary Fig. 36).

The CO₂RR performance and cathodic EE_{C₂H₄} are displayed in Fig. 5b. For C₂₊ species, the FEs increase from 62.3 ± 1.4% (at -0.63 V) to 85.4 ± 2.0% (at -0.81 V) and then drop to 69.3 ± 3.2% (at -1.01 V) due to the increased hydrogen generation at a large overpotential. Remarkably, the selectivity towards C₂H₄ is incredibly high (~99%) among C₂₊ products. There is a small amount of ethanol and negligible acetate in the liquid products and no ethane in the gas products (Supplementary Figs. 37 and 38). The maximum FE_{C₂H₄} and cathodic EE_{C₂H₄} are 84.5 ± 1.7% and 47.6 ± 1.0%, respectively (at -0.81 V), some of the highest FE_{C₂H₄} and cathodic EE_{C₂H₄} values ever reported in the literature (Supplementary Table 2). The active C₂H₄ production is attributed to the stable nanostructure and the Cu/Cu⁺ interfaces (Supplementary Figs. 40 and 41). Moreover, the excellent C₂H₄ selectivity does not compromise the current densities. The C₂H₄ partial current densities are 92.5 mA cm⁻² at -0.81 V and 175.2 mA cm⁻² at -1.01 V, respectively, indicating the high intrinsic CO₂RR activity of the DVL-Cu@GDL catalyst (Supplementary Fig. 42). By comparison, H₂ production, the dominant by-product, is severely suppressed in the flow cell, with a FE of 12.6 ± 1.3% (13.8 mA cm⁻²) at -0.81 V, probably due to the high local pH generated by fast proton consumption and the low buffering capability of the KCl electrolyte.

The CO₂RR performance of the two-electrode flow cell configuration was also tested (Fig. 5c and Supplementary Fig. 31). With increasing current density, the voltage increases linearly between -2 and -5 V. At the optimal current density of 75 mA cm⁻², the 77.3% FE_{C₂H₄} coupled with a full-cell voltage of -3.1 V realized an EE_{C₂H₄} of 28.9 ± 1.3%, the highest value achieved in the neutral catholyte in the literature. Surprisingly, the DVL-Cu@GDL catalyst presented an average FE_{C₂H₄} of 74.0% at a constant current density of 150 mA cm⁻² for ~55 h of stable electrolysis without any surface hydrophobic treatment (Fig. 5e and Supplementary Fig. 39). The compact evaporated Cu film and stable nanostructure might have the ability to prevent the GDL from flooding during electrolysis, which accounts for the excellent long-term stability in the flow cell. Furthermore, to improve the EE_{C₂H₄} at a high current density >200 mA cm⁻², we tested our catalyst in a membrane electrode assembly (MEA) electrolyzer (Fig. 5d and f, Supplementary Fig. 43). The full-cell EE_{C₂H₄} increased markedly to 27.6 ± 0.8% at 200 mA cm⁻² and 23.7 ± 1.1% at 250 mA cm⁻² using 0.5 M KHCO₃ as the anolyte, with competitive FE_{C₂H₄} values of 80.0 ± 2.2% and 71.2 ± 3.3%, respectively. In conclusion, the DVL-Cu catalyst realized cost-effective and stable ethylene conversion at a competitive current density.

Mechanism analysis. To unravel the intrinsic origin of the high structural stability of DVL-Cu, the electrode current density and electrolyte current density of DVL-Cu and Cu₂O nanocubes (12 nm in length) during the CO₂RR were acquired by COMSOL multiphysics simulations (Fig. 6). Cu₂O nanocubes were chosen as a comparison to show the agglomeration effect, and DVL-Cu carefully preserved its nanostructures after the CO₂RR process (Supplementary Fig. 22). Under an identical total circuit current (100 mA cm⁻²), Cu₂O nanocubes deliver a nearly 5-fold higher

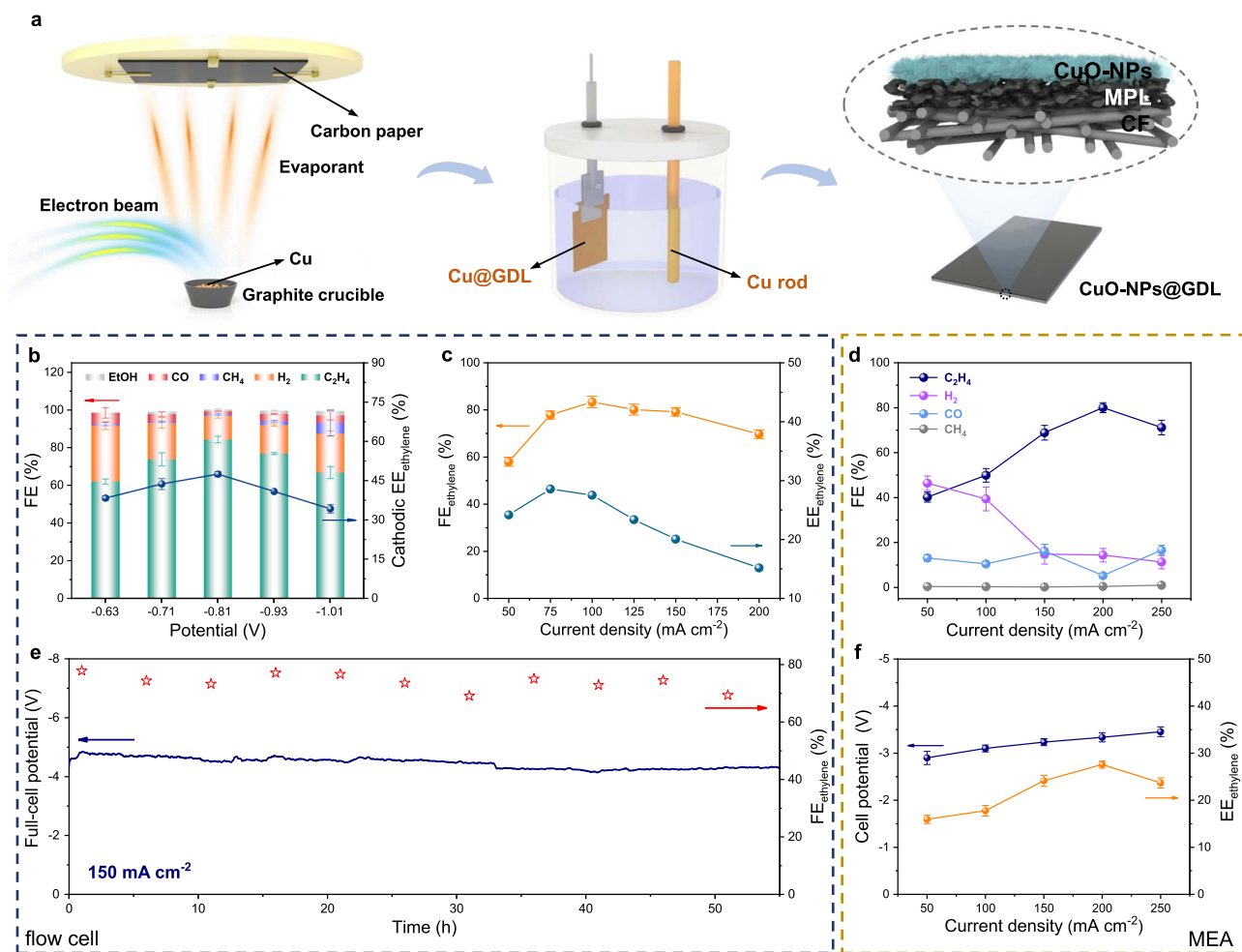


Fig. 5 Preparation and CO₂RR performance of DVL-Cu@GDL in the flow cell and MEA electrolyzer. **a** Schematic illustration of the fabrication of CuO-NPs@GDL. (MPL: microporous layer; CF: carbon fiber) **b** FEs and cathodic EE_{C₂H₄} of the DVL-Cu@GDL catalyst in the flow cell. **c** Full-cell potential and cathodic EE_{C₂H₄} of the DVL-Cu@GDL catalyst in the flow cell. **d** Gas product FEs of the DVL-Cu@GDL catalyst in an MEA electrolyzer. **e** Stability test of the DVL-Cu catalyst at a constant current density of 150 mA cm⁻² in the flow cell. **f** Cell potential and EE_{C₂H₄} of the DVL-Cu@GDL catalyst in an MEA electrolyzer. Error bars represent the standard deviation of three independent measurements.

electrode current density than DVL-Cu (Fig. 6c, d). Uniformly distributed nanoplates with a large surface area of DVL-Cu effectively disperse the current density, which guarantees structural stability during the CO₂RR. Moreover, the electrolyte current density (correlated to local electrostatic intensity) in the Cu₂O nanocube system is more nonuniform than that in the DVL-Cu system and is especially higher at the corners of the nanocubes (Fig. 6a, b). A faster dissolution/redeposition process occurs in those regions with a higher electrolyte current density, and increased local electrostatic intensity leads to easier electromigration of nanostructures, which results in eventual agglomeration of Cu₂O nanocubes. Simultaneously, the higher electrode current density of Cu₂O nanocubes accelerates this agglomeration process. These simulation results indicate that a moderate electrode current density coupled with the uniformly distributed electrolyte current density of DVL-Cu guarantees its prolonged structural stability during the CO₂RR.

The role of local pH and Cl⁻ in the catalytic performance was investigated by electrolyte analysis. KCl (non-buffering electrolyte), KHCO₃ (buffering electrolyte) and K₂SO₄ (non-buffering electrolyte without Cl⁻) were chosen for comparison. A higher local pH was generated when non-buffering electrolytes were used as catholytes due to their poor pH stabilization capability. By observing the overall product distribution, it is found that the

ethylene production in the presence of KHCO₃ is not satisfactory, with significantly higher methane production (Supplementary Fig. 23, detailed analyses are shown in Note 1). It is suggested that the lower local pH in KHCO₃ electrolyte than that in KCl electrolyte results in inferior ethylene production because lower pH regions favor hydrogen evolution and methane production, both needing H⁺⁵⁰. After comparing the catalytic performance in KCl and K₂SO₄, we conclude that the existence of Cl⁻ suppresses hydrogen evolution, especially at high overpotentials, which is considered the result of the Cl⁻-specific adsorption. The strongly adsorbed Cl⁻ facilitates electron transfer from the electrode to CO₂ and suppresses the adsorption of protons, leading to a higher hydrogen evolution overpotential⁵¹.

The long-term stability test results in different electrolytes are also quite informative. Interestingly, DVL-Cu delivered an ~50 h stable current density and ethylene FE in K₂SO₄ under -0.8 V. In comparison, it only preserved stable performance for less than 10 h in KHCO₃ under the same conditions. SEM and TEM images of the post-CO₂RR sample in K₂SO₄ (Supplementary Fig. 24) display morphology and Cu(0)/Cu(I) interfaces equivalent to those obtained from the KCl sample, indicating that a high local pH plays a critical role in the prolonged stability, rather than morphology. Detailed post-electrolysis characterizations were performed to determine the stability origin for the samples obtained

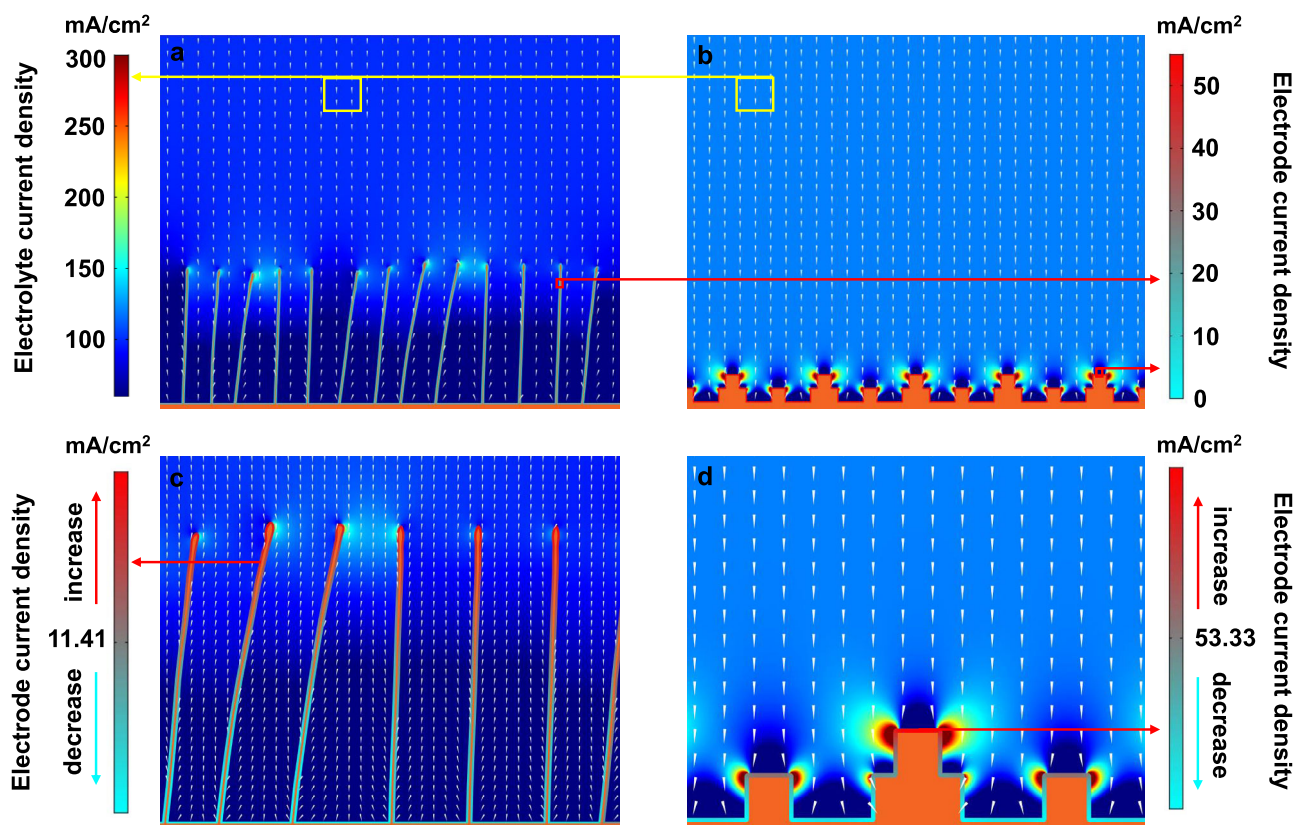


Fig. 6 COMSOL multiphysics simulations. **a, c** Electrode current density and electrolyte current density distribution of DVL-Cu at 100 mA cm^{-2} . **b, d** Electrode current density and electrolyte current density distribution of Cu_2O nanocubes at 100 mA cm^{-2} . The electrode current density and electrolyte current density (in **a** and **b**) correspond to the left and right legends, respectively. The electrode current densities in (**c**) and (**d**) correspond to the left and right legends, respectively. The conical arrows represent the electrolyte current density vector.

from KHCO_3 and KCl. EELS mapping of the KHCO_3 sample (Supplementary Fig. 26) reveals that Cu(I) species agglomerate on the top of nanoparticles, while these species distribute uniformly in the KCl sample (Supplementary Figs. 27 and 28). AES depth profile analyses (Supplementary Fig. 29) further verify the Cu(I) species distribution differences, where the Cu(I) content in the KCl sample is higher with depth than that in the KHCO_3 sample. Apparently, non-buffering electrolytes stabilize the DVL-Cu catalyst by protecting its Cu(0)/Cu(I) interfaces during electrolysis. Since the K_{sp} of CuOH is relatively low (1.0×10^{-14}), a high local pH significantly slows the dissolution of Cu(I) species. Hence, a high local pH suppresses the dissolution/redeposition of Cu(I) species in non-buffering electrolytes, which preserves the Cu(0)/Cu(I) interfaces during the CO_2RR .

To gain mechanistic insights into the CO_2RR catalytically active sites and reaction pathway of DVL-Cu, we further performed DFT calculations to investigate the energy barrier for the production of C_2H_4 and other products at different Cu-containing sites. Here, Cu(110) and $\text{Cu}_2\text{O}(110)$ slabs were first constructed as the model of Cu^0 and Cu^+ catalytic sites based on the STEM and GI-XRD results, and Cu(110) was considered the corresponding active plane to produce C_{2+} products in reference²⁵. The Cu(110)/ $\text{Cu}_2\text{O}(110)$ interface was modeled by distributing the $\text{Cu}_2\text{O}(110)$ slab on the surface of the Cu(110) slab (Supplementary Figs. 44–46, the size effect of Cu_2O slab is discussed in Supplementary Fig. 47, Supplementary Table 1 and Supplementary Note 3). Then, the energy barrier of each step in the reaction pathway on the Cu(110) slab, $\text{Cu}_2\text{O}(110)$ slab and Cu(110)/ $\text{Cu}_2\text{O}(110)$ interface was calculated to evaluate the catalytic performance of different catalytic sites in DVL-Cu.

First, the C_2H_4 formation pathway through the $^*\text{CO}-^*\text{COH}$ dimerization pathway was investigated to reveal catalytic sites on DVL-Cu (Supplementary Tables 4 and 5). The $^*\text{CO}-^*\text{COH}$ dimerization pathway was confirmed to be most favorable over other pathways considering the reaction energy and kinetic adsorption structure (Fig. 7a and Supplementary Figs. 48–50). The reduction of $^*\text{CO}_2$ to $^*\text{COOH}$ occurs with $\Delta G = 0.50 \text{ eV}$ on Cu(110)/ $\text{Cu}_2\text{O}(110)$, which is lower than that on Cu(110) ($\Delta G = 0.76 \text{ eV}$) and Cu_2O ($\Delta G = 1.05 \text{ eV}$) since the interfaces promote the stabilization of the $^*\text{COOH}$ intermediate. Therefore, Cu(110)/ $\text{Cu}_2\text{O}(110)$ secures a higher surface $^*\text{CO}$ coverage, which is consistent with the higher FE_{CO} of DVL-Cu at a low overpotential. More importantly, the energy barriers for the rate-determining step (RDS) are 0.60 eV ($^*\text{CO} + ^*\text{CO} \rightarrow ^*\text{CO} + ^*\text{COH}$), 1.19 eV ($^*\text{CO} + ^*\text{CO} \rightarrow ^*\text{CO} + ^*\text{COH}$) and 1.05 eV ($^*\text{OH}_2\text{CCH} \rightarrow ^*\text{O} + \text{C}_2\text{H}_4$) on Cu(110)/ $\text{Cu}_2\text{O}(110)$, Cu(110) and $\text{Cu}_2\text{O}(110)$, respectively (Fig. 7b, c). Hence, C_2H_4 production happens more easily on the Cu(110)/ $\text{Cu}_2\text{O}(110)$ interface, indicating that these interfaces are the catalytically active sites in DVL-Cu. Furthermore, DFT calculations reveal that the adsorption energy of the $^*\text{OCCOH}$ intermediate is -0.77 eV on Cu(110)/ $\text{Cu}_2\text{O}(110)$, which is more negative than that on Cu(110) (-0.18 eV) and $\text{Cu}_2\text{O}(110)$ (-0.28 eV) (Fig. 7c). These results verify that the presence of heterointerfaces are beneficial to the adsorption of the post-dimerization intermediate ($^*\text{OCCOH}$), thus reducing the energy barrier of C–C dimerization. The carbonyl C binding to the interface while the hydroxyl C binding to Cu atoms is the optimized adsorbed structure of the $^*\text{OCCOH}$ intermediate on the Cu(110)/ $\text{Cu}_2\text{O}(110)$ interface (Fig. 7d). Moreover, C_2H_4 desorption is important for the regeneration of

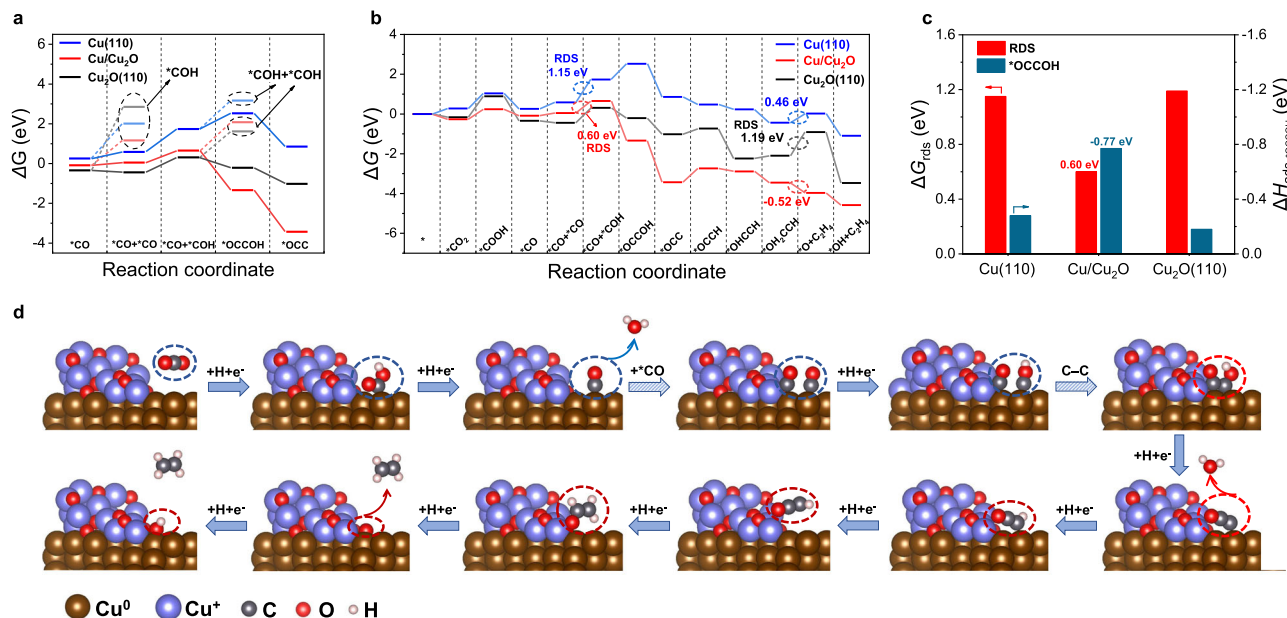


Fig. 7 DFT calculation results. **a** A reaction energy diagram for the CO₂RR to *COH (the intermediate of CH₄ formation) and to *OCC through different dimerization pathways on the Cu(110) slab, Cu/Cu₂O interface and Cu₂O(110) slab. **b** A reaction energy diagram for the CO₂RR to C₂H₄ on the Cu(110) slab, Cu/Cu₂O interface and Cu₂O(110) slab. **c** The free energy of the rate-determined step for the CO₂RR to C₂H₄ pathway and the adsorption energy of the *OCCOH intermediate on the Cu(110) slab, Cu/Cu₂O interface and Cu₂O(110) slab. **d** Optimized structures for the reaction intermediates of the C₂H₄ formation pathway on the Cu/Cu₂O interface.

active sites, which is crucial for the production rate of C₂H₄. Interestingly, this step is exergonic only on Cu(110)/Cu₂O(110) (−0.52 eV), indicating that DVL-Cu possesses a fast C₂H₄ production capacity.

The high selectivity towards C₂H₄ was then studied by comparing the free energy barriers of different catalytic products. The formation of CH₄ via different pathways was primarily considered. As shown in Supplementary Fig. 51, CH₄ production related to the *HCOO intermediate is energetically less favorable than other pathways (leading to CH₄ or other products) related to the COOH* intermediate in the first hydrogenation step on Cu(110)/Cu₂O(110). Based on the *COOH intermediate, the free energy barriers of the second hydrogenation step are 1.57 eV (*HCOOH) and −0.32 eV (*CO) on the Cu/Cu₂O interface, respectively, which indicates that *CO tends to form more than the *HCOOH intermediate. Afterwards, insurmountable energy barriers are required for the hydrogenation of *CO to form *COH on three catalytic sites, while the free energy required for another *CO adsorption step is lower than that for *CO hydrogenation on all three sites, making the reaction pathway to C₂₊ products possible. These factors account for the high C₂H₄/CH₄ product ratios of the DVL-Cu catalyst. Otherwise, the energy barriers required for H₂, formate and C₂H₅OH are dramatically larger than that for C₂H₄ (Supplementary Figs. 51–53). Hence, the formation of C₂H₄ is energetically more favorable than other products, as demonstrated by DFT calculations, which is identical to the CO₂RR product analysis results.

In brief, the adsorption of two *CO species, followed by hydrogenation of one of the *CO species and the consecutive dimerization of *CO and *COH to form *OCCOH, is considered the most favorable pathway for C₂H₄ production on the Cu(110)/Cu₂O(110) interface in DVL-Cu. The insurmountable energy barrier for the hydrogenation of a single adsorbed *CO and the facile C₂H₄ formation pathway on the Cu(110)/Cu₂O(110) interface result in the high C₂H₄/CH₄ ratio in CO₂RR products. These DFT results suggest that the existence of Cu/Cu₂O

interfaces reduces the energy barrier of C–C dimerization and accelerates the desorption of C₂H₄, leading to highly active and selective C₂H₄ production on DVL-Cu.

Discussion

In summary, we have proposed an anodic oxidation method for the large-scale preparation of oxide-derived Cu catalysts with stable Cu/Cu₂O interfaces for highly active CO₂RR to C₂H₄ with high FE and prolonged stability. The high oxidation degree of Cu foil with vertically arranged Cu nanoplates prevents the agglomeration of nanostructures and preserves stable Cu/Cu₂O interfaces during the CO₂RR. Utilizing these advantages, the DVL-Cu catalyst achieves a high FE_{C₂H₄} of 84.5 ± 1.7% and EE_{C₂H₄} of 28.9 ± 1.3% in the flow cell and 27.6 ± 0.8% EE_{C₂H₄} at 200 mA cm^{−2} in the MEA electrolyzer. Moreover, the DVL-Cu catalyst maintains consistent electrolysis performance for ~55 h in the flow-cell. Mechanism analysis indicates that a moderate electrode current density and uniform electrolyte current density coupled with high local pH guarantee structural and interfacial stability, while Cl[−]-specific adsorption suppresses hydrogen evolution at higher overpotentials. DFT calculations reveal that the energy barrier for C–C coupling is significantly reduced because Cu⁺ species enhance the adsorption capacity of the *OCCOH intermediate. The good selectivity, prolonged stability and facile production of the DVL-Cu catalyst highlight its application potential in realizing the industrial conversion of CO₂ to C₂H₄.

Methods

DFT calculations. All DFT calculations were performed using Vienna ab initio simulation package (VASP)⁵², within the projector-augmented wave (PAW) potentials⁵³ together with the generalized gradient approximation (GGA) exchange–correlation⁵⁴ proposed by Perdew–Burke–Ernzerhof (PBE)⁵⁵ to calculate the correlation energies. The bulk-unit cells for pure Cu and Cu₂O were constructed and the k-mesh were 19 × 19 × 19 and 7 × 7 × 10, respectively. The Cu(110) surface, a main exposed facet in the experimental result, was composed of four layers with 3 × 3 supercells, and the Cu₂O(110) supported on Cu(110) surface was modeled by adding Cu₂O(110) clusters of 8 Cu₂O to the Cu(110) surface. The

bottom two layers of Cu(110) were fixed and the vacuum space was set as 20 Å to avoid interactions with their periodic images. The $3 \times 5 \times 1$ Monkhorst–Pack k-point meshes and plane-wave cutoff energy of 520 eV were used in all calculations. The convergence tolerances for residual force and energy were set to 0.01 eV Å⁻¹ and 10⁻⁵ eV, respectively.

Preparation of the catalysts. For the DVL-Cu catalyst used in the H-cell, Cu foils (Alfa Aesar, 0.025 mm, 99.8%) were cut into 1.5 × 3 cm² and annealed at 1050 °C for 3 h under Ar/H₂ atmosphere to remove the copper oxide layer on it. Then the Cu foil was fixed onto a platinum electrode clip to form a working electrode. The counter electrode was a Cu rod made from curled Cu foil. The electrolyte used for anodic oxidation was 1.0 M NaOH (Alfa Aesar, 98%). Galvanostatic oxidation on the Cu foil at a constant current density of 0.26 mA cm⁻² was performed by a CHI 760E potentiostat until the surface of Cu foil entirely turned into black. The CuO-NPs were washed five times by deionized water before being used as the CO₂RR catalyst. For the R-CuO-NPs catalyst, the CuO-NPs were annealed at 450 °C for 3 h under Ar/H₂ atmosphere.

For the DVL-Cu@GDL catalyst used in the flow cell, a 500 nm thick Cu layer was primarily deposited on the carbon paper (Sigracet 28 BC) by an electron beam evaporation system (DZS500, SKY). During the evaporation process, 100 g Cu particles were placed in a graphite crucible inside the evaporation chamber. The chamber pressure was vacuumized to 10⁻⁶ Torr by the molecular pump. A thin Cu layer was deposited on carbon paper at an evaporation rate of 1 Å s⁻¹ controlled by the film thickness measurement system. GDL was kept rotating at a slow speed of 50 rpm during evaporation. Evaporated carbon paper was fixed onto a platinum electrode clip to form a working electrode. The electrochemical oxidation process was the same as the Cu foil except that the current density was 0.13 mA cm⁻² for the carbon paper.

Materials characterization. SEM images were taken by a ZEISS SUPRA55 microscope. A JEOL F200 microscope was used to take the TEM images. AFM images were obtained by Bruker Dimension FastScan microscope. Aberration corrected STEM imaging and EELS mapping were acquired from a Nion HERMES-100 under 100 kV with a 30 mrad convergence angle. The enlarged STEM-BF image is denoised by low-pass filtering. Cu valence state analysis was performed by multiple linear least squares (MLLS) fitting in the 920–960 eV energy-loss range. The processed EELS data has been calibrated along the energy-loss axis to match the standard data⁵⁶, as the as-acquired spectra deviate slightly due to the small non-linearity of the energy dispersion at the two ends of the spectrometer prism. XPS spectra (ESCALAB 250Xi, Thermo Fisher Scientific Inc., USA) was used to investigate chemical compositions and elemental oxidation states of the catalysts. Raman spectra were obtained from the Raman spectrometer (Horiba, Olympus microscope) with a 532 nm laser. GI-XRD patterns were obtained by a Panalytical Empyrean X-ray diffractometer. Gas products were analyzed by a Shimadzu GC 2030 gas chromatograph. Liquid products were analyzed by a NMR spectroscopy (AVANCE III 600 M, Bruker).

Electrochemical CO₂ reduction measurements. A gas-tight electrolysis H-cell (Gaoss Union, 50 mL) separated by a Nafion 117 membrane (Sigma Aldrich) was used to measure the CO₂RR performance of the catalysts. 30 mL 0.5 M KCl (Sigma Aldrich) was employed as catholyte and anolyte. Before CO₂RR test, 500 standard cubic centimeters per minute (sccm) CO₂ (99.999%, Praxair) was constantly bubbled into the electrolytes for 30 min to saturate it with CO₂. A Pt foil (Pine Instruments, 1 × 1 cm²) and a Ag/AgCl electrode (Gaoss Union) filled with saturated KCl solution were used as counter electrode and reference electrode, respectively. We kept the CO₂ flow rate at 20 sccm and 1000 rpm stirring of the catholyte during the CO₂RR. For the long-term CO₂RR stability test, the CO₂-saturated KCl electrolytes were replaced each 12 h. The electrolysis was performed by a CHI 760E potentiostat using chronoamperometry method at each applied potential for 1 h to measure the FE of each product. All applied potentials were converted to the RHE by the equation: E (vs. RHE) = E (vs. Ag/AgCl) + 0.204 V + 0.0591 V × pH - iR , with iR compensation. The gas products combined with CO₂ gas were injected into a six-way valve, which is linked with an online GC-BID. The gas chromatography was calibrated by five standard gases (H₂, CO, CH₄, C₂H₂, C₂H₄ and C₂H₆ in CO₂) with gradient concentrations at 20 sccm flow rate before using. The gas samples were analyzed at least after 30 min electrolysis to insure the CO₂RR reaching a stable state. Liquid samples were collected after 1 h electrolysis and measured by ¹H NMR with dimethyl sulfoxide (DMSO) as an internal standard. The Faradaic efficiencies (FEs) were calculated on the basis of the following equation:

$$\text{Faradaic efficiencies} = \frac{Q_x}{Q_{\text{total}}} = \frac{n_x N_x F}{Q_{\text{total}}} \quad (1)$$

where Q_x and Q_{total} was the charge passed into product x and totally passed charge (C) during CO₂RR, n_x represents the electron transfer number of product x , N_x was the product amount (mol) of x measured by GC or NMR and F was the Faraday constant (96485 C mol⁻¹).

The (cathodic) energy efficiencies were calculated on the basis of the following equation:

$$\text{energy efficiencies} = \frac{E^\ominus}{E_{\text{applied}}} \times \text{FE}_{\text{C}_2\text{H}_4} \quad (2)$$

$$\text{cathodic energy efficiencies} = \frac{E^\ominus}{1.23 \text{ V} - E_{\text{applied}}} \times \text{FE}_{\text{C}_2\text{H}_4} \quad (3)$$

where E^\ominus is the thermodynamic potential for the ethylene formation (1.15 V), E_{applied} represents the potential applied during the CO₂RR.

For the electrochemical CO₂RR test in a flow cell, a commercial flow cell electrolyzer (Gaoss Union, 1 cm² active area) was used. The CuO-NPs@GDL was placed between the gas chamber and catholyte chamber, and the catholyte and anolyte chambers were separated by an anion-exchange membrane (FAA-3-PK-130, Fumapem). A Ag/AgCl (filled with saturated KCl solution) electrode and a Ni foam with NiFe hydroxides deposited on it using an electrodeposition method reported previously⁵⁷ were employed as reference electrode and counter electrode, respectively. KCl and KOH solution were served as the catholyte and anolyte, respectively. The gas flow rate was 50 sccm during CO₂RR and the gas products were injected into a six-way valve. The catholyte and anolyte were circulated by a peristaltic pump at 10 sccm and 200 sccm, respectively. The electrolysis of the flow cell was performed on a potentiostat (CS-150CN, CorrTest) equipped with a 2 A current booster.

For the electrochemical CO₂RR test in an MEA electrolyzer, a commercial MEA electrolyzer (Shanghaikeqi, 5 cm² active area) was used. The CuO-NPs@GDL, an anion-exchange membrane (Sustainion® X37-50) and Ti-IrO₂ mesh were compressed to form MEA. The MEA was placed between the anode chamber and cathode chamber, then assembled together using associated bolts. 0.5 M KHCO₃ solution was served as the catholyte. The gas flow rate was 50 sccm during CO₂RR and the gas products were injected into a six-way valve. The catholyte was circulated by a peristaltic pump at 200 sccm. The electrolysis of the MEA electrolyzer was performed on a potentiostat (HSP-3010, Henghui).

ECSA measurements. The electrochemical double-layer capacitance method was used for ECSA measurements. In a typical procedure, the catalysts were reduced at -0.6 V vs. RHE for 2 min and cyclic voltammograms at different scan rates (20, 40, 60, 80 and 100 mV s⁻¹) have been obtained in Ar-saturated 1 M KOH solution in the non-Faradaic region (-0.07 to 0.13 V vs. RHE) when the curves of different cycles overlapping. The difference between anodic current and cathodic current at 0.03 V of different scan rates was recorded and plot against the scan rates. The 1/2 slope values of these curves were calculated as the double-layer capacitance for corresponding catalysts. The ratios of the double-layer capacitance of the catalysts versus the electropolished copper foil were calculated as the RF⁵⁸.

COMSOL multiphysics simulations. A two-dimensional finite element model was developed to describe the difference of current density distribution between plate electrode and square electrode. A two-dimensional cross-section of 1000 × 800 nm near the electrode was taken for the computational domain. The slice electrodes are represented by thin irregular columns, while the cube electrodes are assumed to be stacked squares. The average height of the sheet electrode is about 300 nm, and the square electrode is about 50 nm.

The tertiary current distribution module from the COMSOL multiphysics software was employed for the finite element simulation. The transport of the K⁺ and the anion was solved by the Nernst-Planck equation:

$$\nabla \cdot \left(D \nabla c_i + \frac{D_{z_i} e}{k_B T} c_i \nabla V \right) = 0 \quad (4)$$

Where c_i is the concentrations of the potassium or anion ion, z_i are the valences of ions, e is the elementary charge, k_B is Boltzmann constant, the absolute temperature T is set as 297.3 K. The reaction current density was obtained by the Butler–Volmer equation:

$$i = i_0 \left[\exp\left(\frac{\alpha_a n F \eta}{RT}\right) - \exp\left(-\frac{\alpha_c n F \eta}{RT}\right) \right] \quad (5)$$

Where the α_a and α_c are the dimensionless anodic and cathodic charge transfer coefficients, respectively. n is the number of electrons involved in the electrode reaction, R is the universal gas constant, F is the Faraday constant. The exchange current density i_0 was obtained by the Arrhenius law:

$$i_0 \propto \exp\left(-\frac{E_a}{k_B T}\right) \quad (6)$$

Where the E_a is the activation energy of the reaction, which was experimentally obtained to be 0.21 eV with K⁺ involved.

Boundary conditions: The upper boundary was set as the electrolyte boundary with a current density at 100 mA/cm², and an ion and anion concentration with 0.5 mol/L. The electrolyte conductivity was assumed to be 10 S/m. The diffusion coefficient of Li⁺ and the anion were set as 5.273 × 10⁻⁹ m²/s and 2.032 × 10⁻⁹ m²/s, respectively.

Data availability

The data supporting this study are available within the paper and the Supplementary Information. All other relevant source data are available from the corresponding author upon reasonable request.

Received: 27 August 2021; Accepted: 15 March 2022;

Published online: 06 April 2022

References

1. Chu, S., Cui, Y. & Liu, N. The path towards sustainable energy. *Nat. Mater.* **16**, 16–22 (2017).
2. Nitopi, S. et al. Progress and perspectives of electrochemical CO₂ reduction on copper in aqueous electrolyte. *Chem. Rev.* **119**, 7610–7672 (2019).
3. Xu, S. & Carter, E. A. Theoretical insights into heterogeneous (photo) electrochemical CO₂ reduction. *Chem. Rev.* **119**, 6631–6669 (2019).
4. Aresta, M., Dibenedetto, A. & Angelini, A. Catalysis for the valorization of exhaust carbon: from CO₂ to chemicals, materials, and fuels. Technological use of CO₂. *Chem. Rev.* **114**, 1709–1742 (2014).
5. Verma, S., Lu, S. & Kenis, P. J. A. Co-electrolysis of CO₂ and glycerol as a pathway to carbon chemicals with improved technoconomics due to low electricity consumption. *Nat. Energy* **4**, 466–474 (2019).
6. Hori, Y., Wakebe, H., Tsukamoto, T. & Koga, O. Electrocatalytic process of CO selectivity in electrochemical reduction of CO₂ at metal electrodes in aqueous media. *Electrochim. Acta* **39**, 1833–1839 (1994).
7. Schouten, K. J. P., Kwon, Y., van der Ham, C. J. M., Qin, Z. & Koper, M. T. M. A new mechanism for the selectivity to C₁ and C₂ species in the electrochemical reduction of carbon dioxide on copper electrodes. *Chem. Sci.* **2**, 1902–1909 (2011).
8. Calle-Vallejo, F. & Koper, M. T. M. Theoretical considerations on the electroreduction of CO₂ to C₂ species on Cu(100) electrodes. *Angew. Chem. Int. Ed.* **52**, 7282–7285 (2013).
9. Jiang, K. et al. Metal ion cycling of Cu foil for selective C–C coupling in electrochemical CO₂ reduction. *Nat. Catal.* **1**, 111–119 (2018).
10. Ma, W. et al. Electrocatalytic reduction of CO₂ to ethylene and ethanol through hydrogen-assisted C–C coupling over fluorine-modified copper. *Nat. Catal.* **3**, 478–487 (2020).
11. Todorova, T. K., Schreiber, M. W. & Fontecave, M. Mechanistic understanding of CO₂ reduction reaction (CO₂RR) toward multicarbon products by heterogeneous copper-based catalysts. *ACS Catal.* **10**, 1754–1768 (2020).
12. Tran, K. & Ulissi, Z. W. Active learning across intermetallics to guide discovery of electrocatalysts for CO₂ reduction and H₂ evolution. *Nat. Catal.* **1**, 696–703 (2018).
13. Liu, X. et al. Understanding trends in electrochemical carbon dioxide reduction rates. *Nat. Commun.* **8**, 15438 (2017).
14. Zhou, Y. et al. Dopant-induced electron localization drives CO₂ reduction to C₂ hydrocarbons. *Nat. Chem.* **10**, 974–980 (2018).
15. Hori, Y., Kikuchi, K. & Suzuki, S. Production of CO and CH₄ in electrochemical reduction of CO₂ at metal electrodes in aqueous hydrogencarbonate solution. *Chem. Lett.* **14**, 1695–1698 (1985).
16. De Luna, P. et al. Catalyst electro-redeposition controls morphology and oxidation state for selective carbon dioxide reduction. *Nat. Catal.* **1**, 103–110 (2018).
17. Weng, Z. et al. Active sites of copper-complex catalytic materials for electrochemical carbon dioxide reduction. *Nat. Commun.* **9**, 415 (2018).
18. Choi, C. et al. Highly active and stable stepped Cu surface for enhanced electrochemical CO₂ reduction to C₂H₄. *Nat. Catal.* **3**, 804–812 (2020).
19. Lv, J.-J. et al. A highly porous copper electrocatalyst for carbon dioxide reduction. *Adv. Mater.* **30**, 1803111 (2018).
20. Zhang, W. et al. Atypical oxygen-bearing copper boosts ethylene selectivity toward electrocatalytic CO₂ reduction. *J. Am. Chem. Soc.* **142**, 11417–11427 (2020).
21. Mistry, H. et al. Highly selective plasma-activated copper catalysts for carbon dioxide reduction to ethylene. *Nat. Commun.* **7**, 12123 (2016).
22. Cheng, T., Xiao, H. & Goddard, W. A. Full atomistic reaction mechanism with kinetics for CO reduction on Cu(100) from ab initio molecular dynamics free-energy calculations at 298 K. *Proc. Natl Acad. Sci. USA* **114**, 1795 (2017).
23. Gao, D. et al. Plasma-activated copper nanocube catalysts for efficient carbon dioxide electroreduction to hydrocarbons and alcohols. *ACS Nano* **11**, 4825–4831 (2017).
24. Weng, Z. et al. Electrochemical CO₂ reduction to hydrocarbons on a heterogeneous molecular Cu catalyst in aqueous solution. *J. Am. Chem. Soc.* **138**, 8076–8079 (2016).
25. Zhu, C. et al. Product-specific active site motifs of Cu for electrochemical CO₂ reduction. *Chem* **7**, 406–420 (2020).
26. Wang, Y. et al. Catalyst synthesis under CO₂ electroreduction favours faceting and promotes renewable fuels electrosynthesis. *Nat. Catal.* **3**, 98–106 (2020).
27. Feng, X., Jiang, K., Fan, S. & Kanan, M. W. Grain-boundary-dependent CO₂ electroreduction activity. *J. Am. Chem. Soc.* **137**, 4606–4609 (2015).
28. Loiudice, A. et al. Tailoring copper nanocrystals towards C₂ products in electrochemical CO₂ reduction. *Angew. Chem. Int. Ed.* **55**, 5789–5792 (2016).
29. Grosse, P. et al. Dynamic changes in the structure, chemical state and catalytic selectivity of Cu nanocubes during CO₂ electroreduction: size and support effects. *Angew. Chem. Int. Ed.* **57**, 6192–6197 (2018).
30. Hall, A. S., Yoon, Y., Wuttig, A. & Surendranath, Y. Mesostructure-induced selectivity in CO₂ reduction catalysis. *J. Am. Chem. Soc.* **137**, 14834–14837 (2015).
31. Yang, K. D. et al. Morphology-directed selective production of ethylene or ethane from CO₂ on a Cu mesopore electrode. *Angew. Chem. Int. Ed.* **56**, 796–800 (2017).
32. Kas, R. et al. Three-dimensional porous hollow fibre copper electrodes for efficient and high-rate electrochemical carbon dioxide reduction. *Nat. Commun.* **7**, 10748 (2016).
33. Zhu, Q. et al. Carbon dioxide electroreduction to C₂ products over copper-cuprous oxide derived from electrosynthesized copper complex. *Nat. Commun.* **10**, 3851 (2019).
34. Hoang, T. T. H., Ma, S., Gold, J. L., Kenis, P. J. A. & Gewirth, A. A. Nanoporous copper films by additive-controlled electrodeposition: CO₂ reduction catalysis. *ACS Catal.* **7**, 3313–3321 (2017).
35. Jin, M. et al. Shape-controlled synthesis of copper nanocrystals in an aqueous solution with glucose as a reducing agent and hexadecylamine as a capping agent. *Angew. Chem. Int. Ed.* **50**, 10560–10564 (2011).
36. Hoang, T. T. H. et al. Nanoporous copper–silver alloys by additive-controlled electrodeposition for the selective electroreduction of CO₂ to ethylene and ethanol. *J. Am. Chem. Soc.* **140**, 5791–5797 (2018).
37. Gao, D., Scholten, F. & Roldan Cuenya, B. Improved CO₂ electroreduction performance on plasma-activated Cu catalysts via electrolyte design: halide effect. *ACS Catal.* **7**, 5112–5120 (2017).
38. Chen, C. S., Wan, J. H. & Yeo, B. S. Electrochemical reduction of carbon dioxide to ethane using nanostructured Cu₂O-derived copper catalyst and palladium(II) chloride. *J. Phys. Chem. C* **119**, 26875–26882 (2015).
39. Zhong, D. et al. Coupling of Cu(100) and (110) facets promotes carbon dioxide conversion to hydrocarbons and alcohols. *Angew. Chem. Int. Ed.* **60**, 4879–4885 (2020).
40. Li, C. W. & Kanan, M. W. CO₂ reduction at low overpotential on Cu electrodes resulting from the reduction of thick Cu₂O films. *J. Am. Chem. Soc.* **134**, 7231–7234 (2012).
41. Yan, Z. et al. The in situ growth of Cu₂O with a honeycomb structure on a roughed graphite paper for the efficient electroreduction of CO₂ to C₂H₄. *Catal. Sci. Technol.* **11**, 6742–6749 (2021).
42. Altaf, N. et al. Electro-derived Cu-Cu₂O nanocluster from LDH for stable and selective C₂ hydrocarbons production from CO₂ electrochemical reduction. *J. Energy Chem.* **48**, 169–180 (2020).
43. Arán-Ais, R. M., Scholten, F., Kunze, S., Rizo, R. & Roldan Cuenya, B. The role of in situ generated morphological motifs and Cu(i) species in C₂₊ product selectivity during CO₂ pulsed electroreduction. *Nat. Energy* **5**, 317–325 (2020).
44. Chen, X. et al. Electrochemical CO₂-to-ethylene conversion on polyamine-incorporated Cu electrodes. *Nat. Catal.* **4**, 20–27 (2021).
45. Pyun, C. H. & Park, S. M. In situ spectroelectrochemical studies on anodic oxidation of copper in alkaline solution. *J. Electrochem. Soc.* **133**, 2024–2030 (1986).
46. Roberts, F. S., Kuhl, K. P. & Nilsson, A. High selectivity for ethylene from carbon dioxide reduction over copper nanocube electrocatalysts. *Angew. Chem. Int. Ed.* **54**, 5179–5182 (2015).
47. Leapman, R. D., Grunes, L. A. & Fejes, P. L. Study of the L₂₃ edges in the 3d transition metals and their oxides by electron-energy-loss spectroscopy with comparisons to theory. *Phys. Rev. B* **26**, 614–635 (1982).
48. Lee, S., Kim, D. & Lee, J. Electrocatalytic Production of C₃–C₄ compounds by conversion of CO₂ on a chloride-induced Bi-Phasic Cu₂O-Cu catalyst. *Angew. Chem. Int. Ed.* **54**, 14701–14705 (2015).
49. Ozden, A. et al. High-rate and efficient ethylene electrosynthesis using a catalyst/promoter/transport layer. *ACS Energy Lett.* **5**, 2811–2818 (2020).
50. Hori, Y., Murata, A. & Takahashi, R. Formation of hydrocarbons in the electrochemical reduction of carbon dioxide at a copper electrode in aqueous solution. *J. Chem. Soc., Faraday Trans. 1* **85**, 2309–2326 (1989).
51. Ogura, K. et al. CO₂ attraction by specifically adsorbed anions and subsequent accelerated electrochemical reduction. *Electrochim. Acta* **56**, 381–386 (2010).
52. Kresse, G. & Furthmüller, J. Efficient iterative schemes for ab initio total-energy calculations using a plane-wave basis set. *Phys. Rev. B* **54**, 11169–11186 (1996).
53. Blöchl, P. E. Projector augmented-wave method. *Phys. Rev. B* **50**, 17953–17979 (1994).
54. Perdew, J. P. & Wang, Y. Accurate and simple analytic representation of the electron-gas correlation energy. *Phys. Rev. B* **45**, 13244–13249 (1992).

55. Perdew, J. P., Burke, K. & Ernzerhof, M. Generalized gradient approximation made simple. *Phys. Rev. Lett.* **77**, 3865–3868 (1996).
56. Ahn, C. C., Krivanek, O. L., Burgner, R. P., Disko, M. M., & Swann, P. R. EELS atlas: a reference collection of electron energy loss spectra covering all stable elements. *Gatan, Inc.* (Warrendale, U.S.A., 1983).
57. Lu, X. & Zhao, C. Electrodeposition of hierarchically structured three-dimensional nickel–iron electrodes for efficient oxygen evolution at high current densities. *Nat. Commun.* **6**, 6616 (2015).
58. Verdaguer-Casadevall, A. et al. Probing the active surface sites for CO reduction on oxide-derived electrocatalysts. *J. Am. Chem. Soc.* **137**, 9808–9811 (2015).

Acknowledgements

This work was supported by the National Key R&D Program of China (Grant No. 2018YFA0306900), the National Natural Science Foundation of China (No. 51872012), the Fundamental Research Funds for the Central Universities and the 111 Project (B17002).

Author contributions

These authors contributed equally: W.L., P.Z., A.L., and B.W. Y.G. and W.Z. conceived the project and supervised the research work. W.L. and P.Z. designed and conducted most of the experiments of this project. A.L. and W.Z. performed the STEM measurements and analyzed the results. B.W. and R.Z. designed the computational studies and analyzed the computational data. G.Z. conducted the GI-XRD measurements. K.S., X.G., and Q.C. performed the electronic beam evaporation. W.L., Y.W. and X.W. co-wrote the manuscript. Y.G., W.Z., and R.Z. discussed the results and reviewed the manuscript.

Competing interests

The authors declare no competing interests.

Additional information

Supplementary information The online version contains supplementary material available at <https://doi.org/10.1038/s41467-022-29428-9>.

Correspondence and requests for materials should be addressed to Yongji Gong.

Peer review information *Nature Communications* thanks Gengfeng Zheng, Ali Seifitokaldani and the other anonymous reviewer(s) for their contribution to the peer review of this work. Peer review reports are available.

Reprints and permission information is available at <http://www.nature.com/reprints>

Publisher's note Springer Nature remains neutral with regard to jurisdictional claims in published maps and institutional affiliations.



Open Access This article is licensed under a Creative Commons Attribution 4.0 International License, which permits use, sharing, adaptation, distribution and reproduction in any medium or format, as long as you give appropriate credit to the original author(s) and the source, provide a link to the Creative Commons license, and indicate if changes were made. The images or other third party material in this article are included in the article's Creative Commons license, unless indicated otherwise in a credit line to the material. If material is not included in the article's Creative Commons license and your intended use is not permitted by statutory regulation or exceeds the permitted use, you will need to obtain permission directly from the copyright holder. To view a copy of this license, visit <http://creativecommons.org/licenses/by/4.0/>.

© The Author(s) 2022